Reid A. Berdanier[1]
Mem. ASME
Department of Mechanical Engineering,
The Pennsylvania State University,
University Park, PA 16802
e-mail: rberdanier@psu.edu

Iván Monge-Concepción
Department of Mechanical Engineering,
The Pennsylvania State University,
University Park, PA 16802

Brian F. Knisely
Department of Mechanical Engineering,
The Pennsylvania State University,
University Park, PA 16802

Michael D. Barringer
Mem. ASME
Department of Mechanical Engineering,
The Pennsylvania State University,
University Park, PA 16802

Karen A. Thole
Mem. ASME
Department of Mechanical Engineering,
The Pennsylvania State University,
University Park, PA 16802

Eric A. Grover
Pratt & Whitney,
East Hartford, CT 06118

Scaling Sealing Effectiveness in a Stator–Rotor Cavity for Differing Blade Spans

As engine development continues to advance toward increased efficiency and reduced fuel consumption, efficient use of compressor bypass cooling flow becomes increasingly important. In particular, optimal use of compressor bypass flow yields an overall reduction of harmful emissions. Cooling flows used for cavity sealing between stages are critical to the engine and must be maintained to prevent damaging ingestion from the hot gas path. To assess cavity seals, the present study utilizes a one-stage turbine with true-scale engine hardware operated at engine-representative rotational Reynolds number and Mach number. Past experiments have made use of part-span (PS) rather than full-span (FS) blades to reduce flow rate requirements for the test rig; however, such decisions raise questions about potential influences of the blade span on sealing effectiveness measurements in the rim cavity. For this study, a tracer gas facilitates sealing effectiveness measurements in the rim cavity to compare data collected with FS engine airfoils and simplified, PS airfoils. The results from this study show sealing effectiveness does not scale as a function of relative purge flow with respect to main gas path flow rate when airfoil span is changed. However, scaling the sealing effectiveness for differing spans can be achieved if the fully purged flow rate is known. Results also suggest reductions of purge flow may have a relatively small loss of seal performance if the design is already near a fully purged condition. Rotor tip clearance is shown to have no effect on measured sealing effectiveness. [DOI: 10.1115/1.4042423]

Introduction

The design of efficient gas turbines continues to be important for both power generation and aviation. Gas turbine thermodynamic efficiencies benefit from increasing pressure ratios and corresponding increases of turbine inlet temperatures. These improvements place additional strains on engine manufacturers since durability issues also follow increasing turbine inlet temperatures. Modern gas turbines operate at temperatures higher than the melting point of engine components, which are alleviated through the use of cooling air bled from the compressor that bypasses the combustor. In addition to cooling the turbine airfoils, there is also concern as to whether there could be migration of the hot main gas flow into regions of the turbine that are not actively cooled, such as the blade under-platform. The high-pressure cooling air bled from the compressor is also used to seal the gaps between stages to prevent hot gas ingestion under the platform. In both cases of turbine airfoil cooling and sealing, minimizing the high-pressure bypass flow is desired to avoid parasitic efficiency losses.

Rim sealing, which affects the platform region between stages, is a cooling technology developed to prevent hot gas ingestion into the wheel-space cavity. Specifically, rim seals are located at the platform interface where both stationary and rotating components meet. The geometry of the rim seal in actual engines is designed to create a complicated flow path that discourages the hot gas from entering into the cavity. The high pressure bypass flow from the compressor provided to this region is known as purge flow. The use of excessive purge flow results in an adverse effect on engine efficiency since it is not used to create any network by the turbine. Therefore, it is critical to build an improved understanding of minimizing purge flow requirements while maintaining sealing performance.

The topic of physics-based models in predicting the minimum purge flow required to fully seal the rim cavity continues to be important. As will be discussed, there are only a few models available for such predictions and most have used very simplified rim seal geometries toward developing the empirical correlations. Often, designers simply refer to the required purge flow rate as a percentage relative to the main gas path flow rate. The unique question that this paper addresses is the validity of referencing the purge flow rate in terms of the main gas path flow rate. Specifically, the results in this paper compare sealing effectiveness measurements in the rim seal between simplified part-span (PS) blade [1] and a full-span (FS) blade while maintaining the same rim seal and rim cavity geometries.

Literature Review

Rim seal geometries are inherently complex to minimize catastrophic hot gas ingestion into the wheel-space cavity of the turbine. Although this is a critically important region of the engine, there are only a few empirical models available for predicting the amount of purge flow required to minimize hot gas ingestion. Since the focus of this paper is to evaluate the scaling of sealing effectiveness for the same wheel-space cavity and airfoil geometry, this literature review specifically discusses past studies that have identified correlations to predict ingestion in rim seals.

A recent review by Scobie et al. [2] outlined previous studies completed on ingestion by several other researchers. Their review paper offers a timely overview of the various ingestion mechanisms that were previously described by Johnson et al. [3]. The

[1]Corresponding author.

Contributed by the International Gas Turbine Institute (IGTI) of ASME for publication in the Journal of Turbomachinery. Manuscript received December 7, 2018; final manuscript received December 24, 2018; published online January 21, 2019. Editor: Kenneth Hall.

various mechanisms described include rotational effects such as disk pumping, external effects due to the unsteady vane and blade pressure fields, and geometry effects due to rim seal design.

Many of the correlations in the literature are empirically based on experiments, such as those conducted by Bayley and Owen [4], using a simple geometry of the wheel space between a rotor and stator. Using two disk configurations, a shrouded disk and an unshrouded disk, Bayley and Owen were able to study ingress and egress fluid dynamics in the region of a rim seal. Their experimental results led to a correlation to determine the minimum amount of flow required to completely purge the rim seal from hot gases in the main gas path. The minimum flow required was found to be independent of the shroud clearance as well as the rotational Reynolds number.

Phadke and Owen [5] studied several basic geometries of generic rim seals. Using flow visualization techniques, they found that the purge flow was entrained by the rotor boundary layer and moved radially outward to preserve the angular momentum; this effect is called disk pumping. The authors explained that the effects of the pressure distribution on the external platform resulting from the upstream vane also affected the ingestion of the hot gas into the rim seal. The data showed that the flow required to purge the rim seals increased with increasing rotational Reynolds number.

Widely accepted orifice equations based on experimental data were developed by Owen [6,7] to predict ingestion over a range of conditions. The orifice model consists of treating the rim seal geometry as an orifice where viscous effects are negligible when compared to inertial effects. The orifice model quantifies the sealing effectiveness in terms of a nondimensional discharge coefficient, which is empirically obtained. Sangan et al. [8,9] derived equations for turbine sealing effectiveness for three cases of ingress. The equations derived by Sangan et al. incorporate an empirically derived discharge coefficient for both ingress and egress. The required minimum flow for a complete purge of the rim seal was determined for externally induced ingress as a function of the peak to trough pressure difference. The minimum flow parameter of the rotationally induced ingress was calculated as a function of a modified internal swirl ratio.

Scobie et al. [10] studied the ingress and egress of a 1.5-stage gas turbine and found that it was possible to quantify the mass fraction of fluid carried over from upstream egress into downstream ingress. They also found that when flow egress was present, there was no significant flow disturbance near the blade platform. The authors measured sealing effectiveness radially in the annulus as well as in the wheel-space cavity in both the stator wall and rotor wall. By this method, doubling the minimum amount of flow required to prevent ingress had no effect in the sealing effectiveness in the wheel-space cavity. Scobie and Hualca used Sangan's [8,9] empirical model, described above, uses an explicit relationship between effectiveness and sealing mass flow. The authors found that Sangan's rim seal effectiveness model fits the experimental data with positive results for both upstream seeding configurations.

Clark et al. [1] tested two purge flow configurations, one with 150-holes and the other with 32-holes for a 1.5-stage turbine at engine-relevant Reynolds number and Mach number. More importantly, the rim seal geometry was representative of a modern turbine design. In their study, the turbine vanes and blades were not full-scale and were also uncooled. The authors were able to demonstrate that the sealing effectiveness increased with increasing purge flows. Measured sealing effectiveness values also increased in the radial direction from the outer rim seal inward; considerable ingestion was found in the wheel-space cavities for very low purge flows. The experiments by Clark et al. showed that of the two configurations tested, the 150-hole configuration was able to completely purge and prevent hot gas ingestion from the main gas path at a high purge flow rate, whereas the 32-holes geometry was not able to purge the rim seal for the same flow rate. Clark et al. also showed that the orifice model by Owen [6,7] scaled the data with mixed results. The model was able to scale the sealing effectiveness found in the outer rim seal. However, the orifice model did not scale the sealing effectiveness at the location of the purge flow injection.

The uniqueness of this study is that sealing effectiveness measurements were made using the same geometry as Clark et al. [1], but with a change of the span of the vanes and blades to full-span airfoils in the current study. The rim cavity geometries (disk, cover plates, labyrinth seals, seal clearance gaps, seal overlaps, etc.) are all identical between the two cases. With the change to full-span vanes and blades, there was a corresponding increase of main hot gas flow rate; all other test conditions were matched. It would be expected that the span of the airfoils would have little to no effect on the sealing effectiveness; however, the question is how best to scale the sealing effectiveness in the two cases. This paper addresses the scaling of required purge flows for sealing effectiveness in relation to varying main gas path flow rates.

Start Facility: Upgrades and Modifications

The research facility and turbine test article described in this paper are located within the Steady Thermal Aero Research Turbine (START) Laboratory at The Pennsylvania State University. The START facility enables research and testing of engine-representative rotating turbine hardware at elevated pressures and temperatures in a continuous-duration environment. Primary goals of the facility include advancing and improving the development of sealing and cooling technologies in the turbine section of gas turbine engines.

Details related to the original facility design were previously described by Barringer et al. [11]. In late 2016 and early 2017, several new upgrades to the rig infrastructure occurred in the START facility to expand the operating capacity, as illustrated in Fig. 1. Specific goals of the expansion included doubling the flow rate, allowing full span airfoil testing, and increasing the temperature of the main gas path to allow improved accuracy of measured

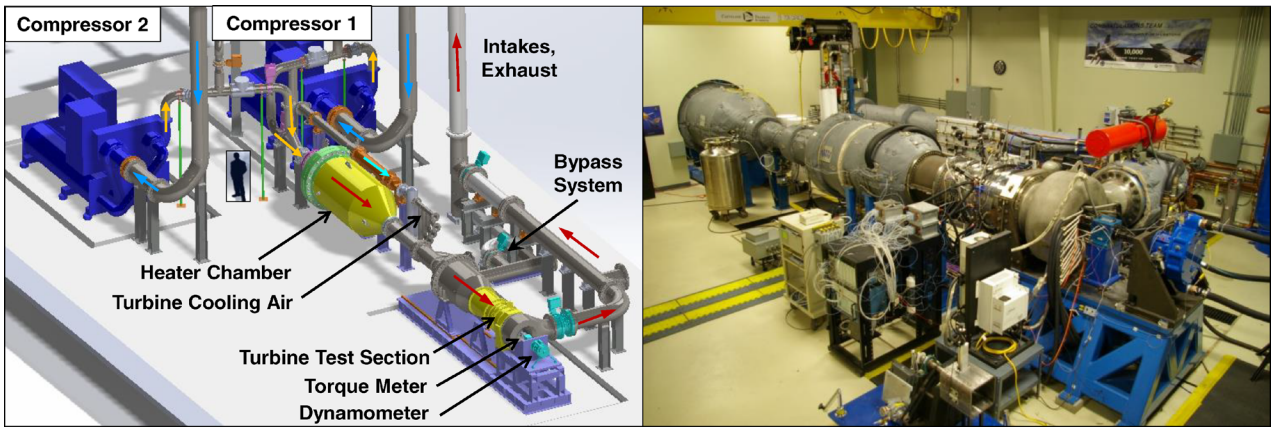

Fig. 1 START facility layout following infrastructure upgrades

airfoil heat transfer [1,12,13]. Furthermore, instrumentation and data acquisition upgrades were completed to improve the accuracy of relevant quantities.

To achieve these goals, the facility was upgraded to include a second air compressor, identical to the first, each powered by a separate 1.1 MW (1500 hp) motor. Each air compressor has an air flow discharge capacity of 5.7 kg/s (12.5 lbm/s) at approximately 480 kPa and 395 K (70 psia and 250 °F), resulting in a total turbine airflow capability of 11.4 kg/s (25.0 lbm/s).

A custom 3.5 MW in-line natural gas heater (see Fig. 1) was installed in the main gas path upstream of the test section, allowing precision control of turbine inlet temperatures beyond the compressor discharge temperature. The wide operating range of the heater provides turbine inlet temperature capability of up to 675 K (750 °F) at the full 11.4 kg/s combined discharge from the tandem compressors.

High-temperature, calibrated Venturi flow meters were installed upstream and downstream of the test turbine section to provide improved accuracy for main gas path flow rate (on the order of 0.4% for flow rates in the present study). A pedestal-mounted phase-shift torque meter was installed in the driveline between the turbine shaft end and the dynamometer (with a continuous rated speed of 12,000 rpm). The torque meter features an accuracy of ±0.12% full scale torque, which yields ±0.84 N·m (0.6 ft-lbf) and contributes to an improved measurement of torque-based turbine stage efficiency.

Overall, recent upgrades to the START facility fulfill many of the facility's original design goals, and they provide the ability to continue research with full-span turbine hardware at elevated air temperatures and pressures. In its current configuration, the test section features a one-stage turbine with a vane-blade configuration, as shown by the cross section in Fig. 2.

Facility Instrumentation and Measurements. The turbine test section is highly instrumented as shown in Fig. 3. A series of circumferentially distributed total pressure and total temperature measurements characterize an inlet plane approximately eight axial chords upstream of the vane. In addition, single-element Kiel head total pressure probes were traversed radially at a location approximately 1.5 axial chords upstream of the vane to further characterize the turbine inlet.

Near-term tests in the START facility are focused on isolating blade cooling effects, and therefore, an uncooled vane is desired. As a result, modifications were made to the vanes to create an uncooled vane configuration by carefully filling the film cooling holes with a two-part high-temperature epoxy to maintain an aerodynamic surface. The engine-representative vanes are combined with four direct metal laser sintered nickel alloy vanes. The direct metal laser sintered vanes were specifically designed to include integrated pressure taps at various locations around the vane. These pressure taps provide the ability to measure pressure and

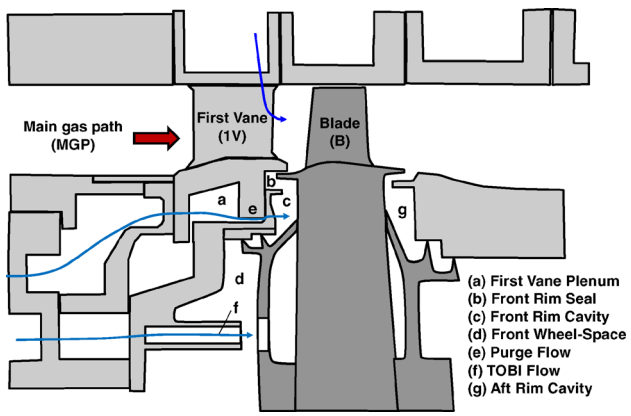

Fig. 2 Turbine flow path cross section

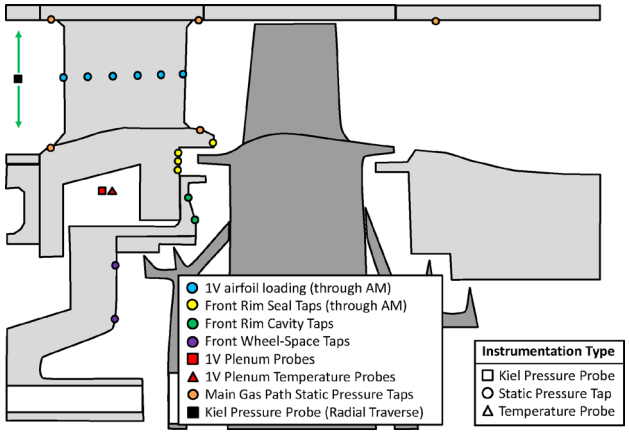

Fig. 3 Test section instrumentation layout

tracer gas (CO_2) concentration in the rim seal region. Although not used in this study, all vanes include a series of holes at the trailing edge, which were left open to provide an aerodynamic boundary condition into the downstream rotor.

The turbine has three independently controlled secondary air supplies, as identified in Fig. 2, which feed the test section including: (1) purge flow from the plenum under the platform of the first stage vane (1V), (2) tangential on-board injection (TOBI) flow, and (3) 1V trailing edge flow. The purge flow provided to the rim cavity region comes from the under-platform vane plenum through a series of purge holes (150 total). To further facilitate a direct comparison with Clark et al. [1], no TOBI flow was introduced for these experiments. Although this TOBI flow was not incorporated for the comparisons presented herein, it is important to note that the rim cavity purge flow may follow a path that leads to the blade cooling holes through the disk cover plate. These film cooling holes were not present in the blades for Clark et al. [1], and the corresponding effects will be discussed.

Representative uncertainties for pertinent parameters are included in Table 1, for which the reference conditions represent the maximum capability of the facility outlined in the Start Facility section. Bias uncertainty in the gas analyzer was reduced by calibrating the gas analyzer using two different known concentrations of CO_2, and precision uncertainty was minimized by calculating an average of data collected from the gas analyzer over a 30 s time window of steady turbine operation.

Gas Concentration. For the results presented in this paper, CO_2 was injected as a tracer gas into the secondary flow system far upstream of the plenum under the vane platform. A detailed description and validation of the measurement technique was provided by Clark et al. [13]. The CO_2 was introduced at a level of 1% (by volume), and the concentration of the tracer gas was measured at various locations in the rim cavity region (see Fig. 4). Ultimately, sealing effectiveness, ε_c, was defined according to

$$\varepsilon_c = (c - c_\infty)/(c_s - c_\infty) \quad (1)$$

Table 1 Uncertainty in facility and turbine measurements

Parameter	Total uncertainty
Main gas path flow rate, $\dot{m}/\dot{m}_{ref}$	±0.004
Shaft rotational speed, Ω/Ω_{ref}	±0.001
Pressures, P/P_{ref}	±0.001
Temperatures, T	±0.4 K
1.0 stage pressure ratio, PR/PR_{ref}	±0.005
Purge flow rate, Φ/Φ_{ref}	±0.018
Sealing effectiveness, ε_c	±0.015 to ±0.025

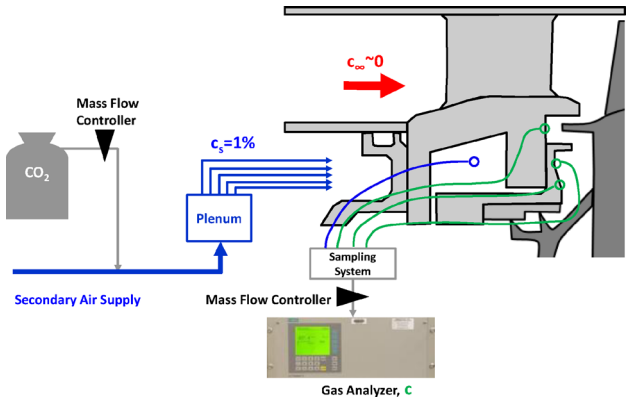

Fig. 4 Schematic of CO_2 injection and sampling system

Table 2 Test turbine operating conditions

Parameter	Value
Density ratio, ρ_P/ρ_{MGP}	1.1–1.5
Vane inlet Mach number	0.1
Vane inlet axial Reynolds number	1×10^5
Blade inlet Mach number	0.7
Blade inlet axial Reynolds number	1.4×10^5
Rotational Reynolds number	$3.5–6.0 \times 10^6$

In Eq. (1), the sealing effectiveness represents the ratio of the difference between CO_2 concentration measured at a given location, c, and the background level, c_∞, to the difference of the supply concentration, c_s, and the background level. For these measurements, the background level was measured by a Kiel-head total pressure probe at midspan in the main gas path upstream of the turbine. As this test turbine operates with standard atmospheric air as the working fluid, the background (ambient) CO_2 concentration level is typically on the order of 400 ppm. Following recommendations outlined by Clark et al. [13], sampling was performed by selecting a gas extraction rate which was sufficiently low, to avoid influencing the flow field (an "isokinetic" condition). Sealing effectiveness was sampled from locations included in Fig. 2. These areas include the front rim seal (b), the rim cavity (c), and the front wheel-space cavity (d).

Turbine Operating Conditions. For the data presented in this study, 150 purge holes provided the under-platform flow. Sealing effectiveness measurements were collected for the full-span hardware over a range of purge flow rates up to approximately 4.5% of main gas path flow rate for comparison with part-span data. Other pertinent conditions are outlined in Table 2. The stability of the facility operating conditions has relative variations of less than 0.4% for continuous operation over several hours.

To further benchmark the facility operating conditions, radial traverses of turbine inlet conditions were collected using an in-house-designed set of radial traversing mechanisms. For these measurements, a total pressure probe with a 1.6 mm (0.063 in.) diameter Kiel was traversed across the annulus. The probes have an acceptance half-angle of more than 40 deg, although the flow is primarily axial through the undisturbed annulus upstream of the turbine.

The inlet pressure traverse data are presented in Fig. 5(*a*) as a normalized pressure versus relative span height, and a representative error bar is shown. These data represent a uniform pressure profile, without any imposed distortion or turbulence generators. For this case, the pressure profile is uniform within 0.01% across the range of 7 to 96% span, with a maximum deviation from uniformity of 0.15% at 100% span. Furthermore, a repeatability study shows two separate tests fall directly on top of one another, signifying the repeatability is an order of magnitude better than the uncertainty of the measurements.

The inlet temperature traverse data were normalized in a similar manner and are presented in Fig. 5(*b*) with the heater operating at a low-temperature setting and without heat addition. Even with a fully insulated inlet section, there is an increased thermal gradient near the outer diameter of the flow path when the heater is on due to additional heat loss through the rig components. Specifically, the air temperature at the wall is 2.5% lower than the average with the heater on, compared to a wall temperature 2% lower than the average with the heater off.

The turbine operating conditions are further defined by the 50% span loading distribution on the first vane, as presented in Fig. 6. The measurements in this figure were collected from two different

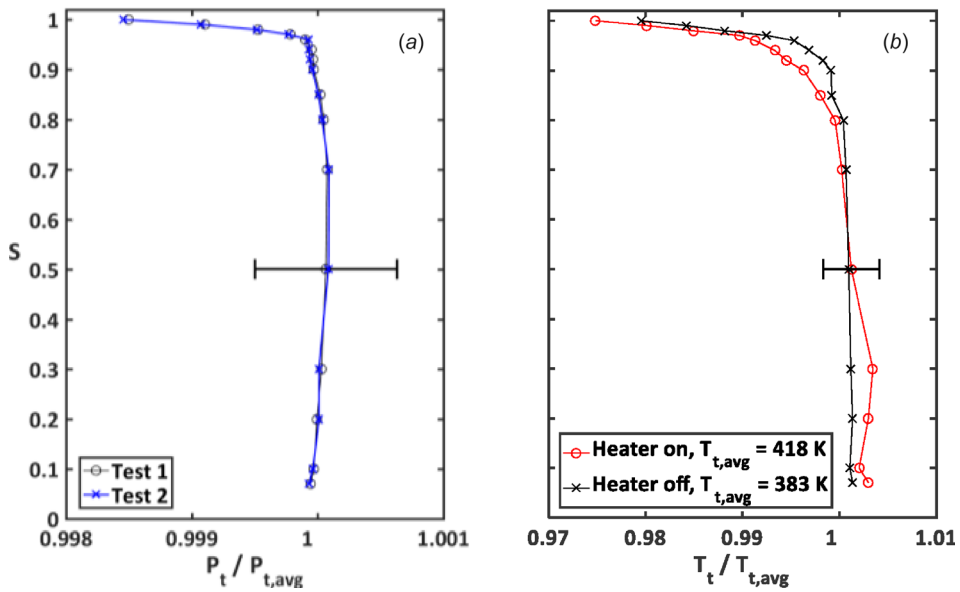

Fig. 5 Radial profiles of test section inlet conditions: (*a*) normalized total pressure and (*b*) total temperature with and without heat addition

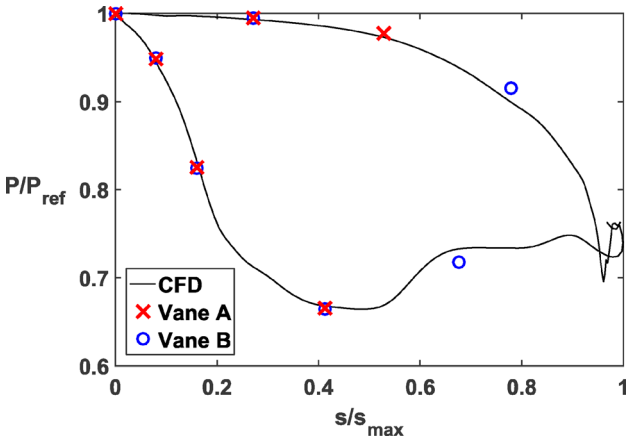

Fig. 6 Normalized vane surface static pressure at 50% span

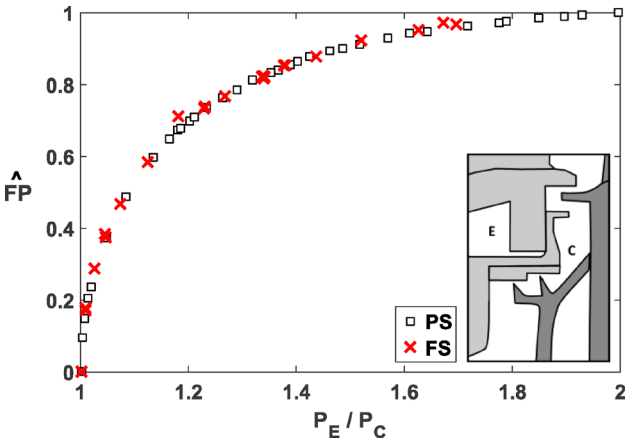

Fig. 7 Normalized flow parameter curves from part-span and full-span configurations. All data collected with nonrotating turbine arrangement.

vanes on opposite sides of the turbine, both of which were manufactured through additive technologies to enable integrated pressure routing. The two aft measurement locations on vane A are not shown because they did not flow through the additively manufactured flow passages. The surface static pressures in Fig. 6 are normalized by a representative turbine inlet pressure and compared with pretest computational fluid dynamics predictions. These results indicate a circumferential uniformity in the test section, which echoes the uniformity observed in the same facility by Clark et al. [1] with a part-span configuration. The comparison of experimental measurements with computational fluid dynamics also highlights the performance agreement of the full-span geometry to the design intent of the flow through the first vane.

Scaling Methods for Effectiveness Data

Data presented by Clark et al. [1] outlined sealing concentration effects for several positions in the rim cavity region for engine-representative seal geometries. Note that the TOBI flows were not included by Clark et al. or the present study. The recent facility modifications enable an evaluation of scaling methods for sealing effectiveness data by a comparison of previous PS blades (with no internal cooling) to current FS blades (with true engine cooling architectures). Prior to evaluating comparisons between these configurations, consistency of purge hole flow capacity was qualified by means of a flow parameter test when the turbine rotor was stationary, Fig. 7. In Fig. 7, the ordinate presents a normalized flow parameter, $\widehat{\mathrm{FP}}$, as a function of pressure ratio across the purge holes. Here, $\widehat{\mathrm{FP}}$ is defined by

$$\widehat{\mathrm{FP}} = \frac{\mathrm{FP}}{\mathrm{FP}_{\mathrm{max,PS}}} \tag{2}$$

where the flow parameter, FP, is a thermodynamic scaling of flow rate with a contribution for the number of purge holes, N

$$\mathrm{FP} = \frac{\dot{m}_{\mathrm{P}}\sqrt{T_{\mathrm{t,E}}}}{P_{\mathrm{t,E}}N} \tag{3}$$

Also, in Eq. (2), $\mathrm{FP}_{\mathrm{max,PS}}$ is the maximum value of flow parameter tested for the part-span configuration.

The part-span data in Fig. 7 are compared with full-span data that were collected after the facility modifications were completed, including a complete rebuild of the turbine test section. Although the blades and vanes were changed, the purge hole frame geometry was retained between the two tests. The qualitative agreement shown in Fig. 7 highlights facility repeatability between builds, and ensures a meaningful comparison of purge flow sealing effectiveness data collected from the different configurations.

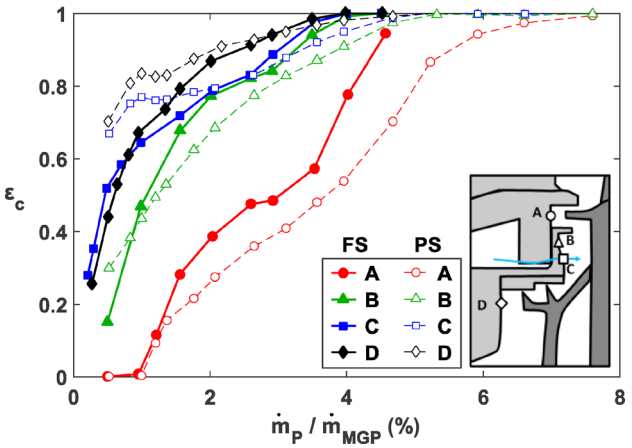

Fig. 8 Sealing effectiveness comparison for FS and PS hardware

Comparisons of seal performance for the PS [1] and FS configurations are presented in Fig. 8, where the sealing effectiveness is shown as a function of relative flow rate (total purge flow normalized by main gas path flow rate)

$$\dot{m}_{\mathrm{rel}} = \frac{\dot{m}_{\mathrm{P}}}{\dot{m}_{\mathrm{MGP}}} \tag{4}$$

Through Fig. 8, several comparisons are drawn. First, the same general trend exists for the FS and PS results such that the effectiveness increases with decreasing radius. However, it is observed that the effectiveness data do not collapse for both blade spans when presented as a function of $\dot{m}_{\mathrm{rel}}$. It is also seen that the relative flow rates at which a fully purged condition occurs do not scale with main gas path flow rate. Table 3 summarizes the

Table 3 Flow rates for fully purged conditions ($\dot{m}_{\mathrm{rel}}$(%))

Location	Part-span	Full-span
A	7.5	4.8
B	5.5	4.0
C	5.0	4.0
D	5.0	4.0

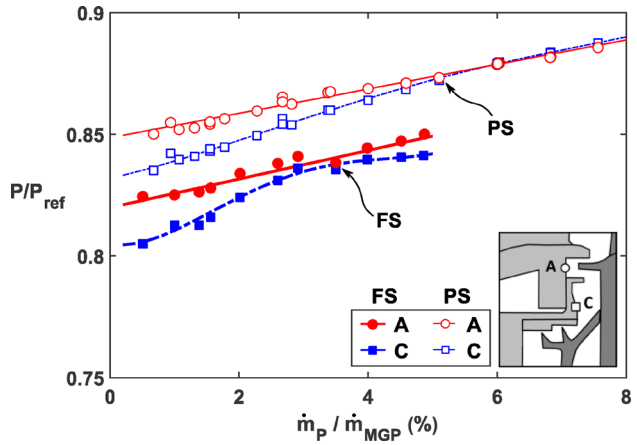

Fig. 9 Nondimensional rim seal and cavity pressures across a range of purge flows for full-span and part-span geometries

relative flow rates at which the locations are fully purged for the part-span and full-span configurations. It should be noted here that location A did not fully purge for the full-span configuration within the range of tested purge flow rates. The value reported in Table 3 is an approximation based on extrapolation from measured data.

The inability to scale purge flow rate with main gas path flow rate due to a change of airfoil span can be described by a fundamental thought experiment: as airfoil heights are increased to be infinitely large resulting in increased main gas path flowrates, it is not expected that the amount of purge flow required for the same sealing effectiveness value would increase in a similar manner. As a result, it is not expected that a direct relationship would exist between sealing effectiveness and $\dot{m}_{\mathrm{rel}}$. However, this observation is of particular value because many engine designers primarily consider cooling flow trends as a percentage of main gas path flow rates.

Also detected more prominently in the FS data shown in Fig. 8 is an inflection point for the sealing effectiveness trend in the rim seal (location A). A similar inflection point is detected for the part-span geometry, but is less apparent. To better understand the inflection point, a series of pressure measurements in the regions of interest were measured as shown in Fig. 9, also as a function of purge flow rate relative to main gas path flow rate, $\dot{m}_{\mathrm{rel}}$.

For both full-span and part-span configurations, Fig. 9 shows linear increase of pressure in the rim seal region (location A), but the rim cavity pressure (location C) follows a nonlinear trend. At very low purge flow rates, the nondimensional rim cavity pressure is approximately 2% lower than the rim seal pressure; this pressure difference facilitates the ingress of main gas path air into the cavity. As the purge flow is increased, though, the rim cavity pressure (location C) increases until it matches the rim seal pressure (location A). This event occurs at a purge flow rate of $\dot{m}_{\mathrm{rel}} \approx 3.5\%$ for the full-span case and $\dot{m}_{\mathrm{rel}} \approx 5\%$ for the part-span case. Both locations are identified by an arrow in Fig. 9.

Referring back to the sealing effectiveness data in Fig. 8, these identified purge flow rates approximately coincide with the identified inflection points in sealing effectiveness, after which a rapid increase of sealing effectiveness occurs. As the pressure in the rim cavity (C) becomes equal with the rim seal (A), the pressure-driven ingestion subsides, so the sharp increase of measured sealing effectiveness is expected. Figure 9 shows further increases of purge flow beyond these identified values follow the rim cavity pressure trending closely with the rim seal region, although rim cavity pressure decreases slightly for the full-span configuration.

As will be discussed later, the pressure level offset between part-span and full-span configurations in Fig. 9 is due to pressure building in the front cavity for the part-span geometry. This effect is due to the absence of film cooling holes in the simplified part-span blades.

Table 4 Relative blade tip clearances

Blade configuration	Clearance ID	$\tau/S(\%)$
Part-span	—	3.8
Full-span	TC1	5.8
Full-span	TC2	3.3

The inability to scale sealing effectiveness by relative main gas path flow rate in Fig. 8 brings rise to a consideration of what potential differences between the part-span and full-span geometries could drive a change in sealing effectiveness. As noted earlier, the rim cavity geometries (disk, cover plates, labyrinth seals, seal clearances, etc.) are all identical between the two cases, and are therefore not variables in this study. As a result, these geometric parameters are not driving the observations in Fig. 8.

It is important to point out that one geometric difference, other than the span dimension, that did occur between the two cases is the size of the tip clearance. The full-span data in Fig. 8 implemented relatively large rotor tip clearance of 5.8% annulus span (TC1) for the full-span geometry, which was not representative of the part-span test conditions. The part-span geometry in Fig. 8 represents a relative rotor tip clearance of approximately 3.8% annulus span as indicated in Table 4. To ensure that this geometric difference was not the cause of the observations in Fig. 8, a turbine flow path change was implemented to decrease the relative tip clearance over the rotor (the same blades were maintained, and only the outer radius of the flow path over the rotor was modified). As outlined in Table 4, the reduced tip clearance gap (TC2) represented a reduced value of 3.3% annulus span, which nearly matched the part-span configuration.

Figure 10 presents sealing effectiveness measurements from the full-span tests at two positions (rim seal, A, and front wheel space, D) for the two rotor tip clearance configurations, TC1 and TC2. Over the range of comparison (up to 3.5% $\dot{m}_{\mathrm{rel}}$), the TC2 data agreed well with TC1. The observed repeatability of measurements, even in the case of a changed rotor tip clearance is well within the uncertainty bands of the measurements. This observation highlights two key takeaways: (1) the differences noted in Fig. 8 are not a result of rotor tip clearance effects, and (2) an increase of rotor tip clearance gap size from 3.3% to 5.8% has no appreciable effect on the measured sealing effectiveness in the rim cavity.

Given that the observed scaling effects on the abscissa of the above figures are not driven by geometric effects, a different approach is utilized to present the sealing effectiveness. For a

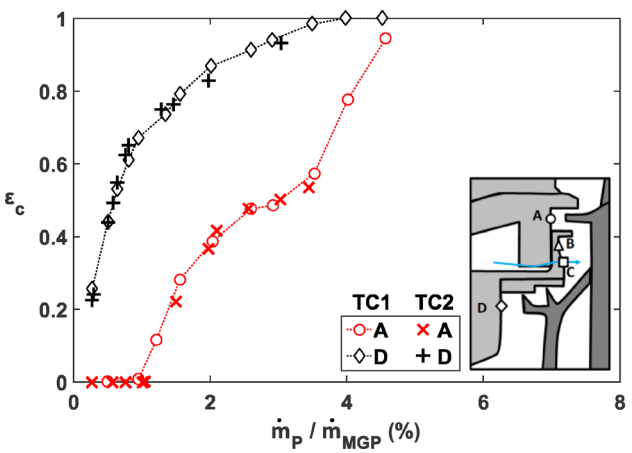

Fig. 10 Sealing effectiveness comparisons for two full-span blade tip clearance configurations

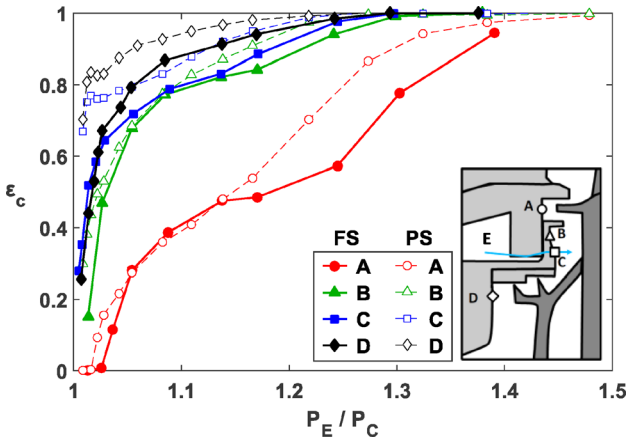

Fig. 11 Sealing effectiveness as a function of pressure ratio across the purge holes

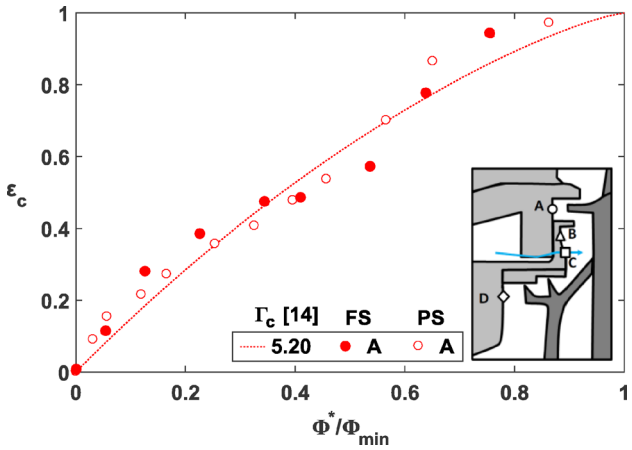

Fig. 12 Empirical model for sealing effectiveness [14] compared with experimental data for rim seal (location A)

given purge hole geometry, the flow rate can be represented by the pressure ratio across the purge holes. This relationship was verified using the flow parameter test introduced above (Fig. 6). Using the pressure ratio as the independent variable, the sealing effectiveness levels are shown in Fig. 11. This pressure ratio is analogous to a momentum flux ratio, characterizing traditional jet in cross-flow studies. In Fig. 11, low flow rates show an improved comparison (up to a pressure ratio of approximately $P_E/P_C \approx 1.15$), especially at the outboard locations (A and B). Beyond this value, however, considerable discrepancies remain between the full-span and part-span configurations. As with Fig. 8, the difference in magnitude of sealing effectiveness for the inboard locations (C and D) also remains as an unresolved discrepancy. This will be addressed further in subsequent discussion.

Comparison With Known Correlations

Following the attempts in Figs. 8 and 11, the values in Table 3 highlight that the full-span and part-span configurations reach a fully purged condition at different relative flow rates (or absolute flow rates). To address this, an alternate approach begins by presenting sealing effectiveness based on nondimensional sealing flow parameter, Φ [14]:

$$\Phi = \frac{\dot{m}_P}{2\pi s_c \rho \Omega b^2} \tag{5}$$

To invoke a comparison with a theoretical prediction for hot gas ingestion, an orifice-based model was chosen [14]. This model calls upon an empirically determined ratio of discharge coefficients for ingress and egress, Γ_c

$$\frac{\Phi^*}{\Phi_{min}} = \frac{\varepsilon}{\left[1 + \Gamma_c^{-2/3}(1-\varepsilon)^{2/3}\right]^{3/2}} \tag{6}$$

The definition of Φ^* as a net sealing flow rate is specific for the observations of this application, which requires accounting of a nonzero flow rate, which yields zero effectiveness.

Through this transformation, the same data for the rim seal (position A) from Fig. 8 are reformulated and combined with the empirically determined discharge coefficient ratio, Γ_c. Considering first the comparison of part-span and full-span data, Fig. 12 shows an improvement in scaling of the data laterally on the abscissa. In fact, the inflections identified in Fig. 8 for both part-span and full-span geometries are collapsed to one common trend in Fig. 12. It should be noted, however, that this improvement noted in Fig. 12 is a result of the normalization by the minimum purge flow rate required to yield a fully purged condition, Φ_{min}, not the change of purge flow representation to sealing flow parameter, Φ.

Similar to the empirically determined discharge coefficient ratio, knowledge of the fully purged flow rate is a requirement for application of the predictive model used in Fig. 12. Although the presentation of normalized sealing flow parameter as the independent variable in Fig. 12 is initially shown for comparison with the predictive model, it also has the added benefit of appropriately scaling the previously discrepant data. Figure 12 shows if the purge flow rate, which yields a sealing effectiveness of unity (fully purged condition) is known, then the behavior across the full range of purge flow rates is defined for any changes to the main gas path geometries.

The rim seal region is of particular importance for engine designers in terms of predictive capability. The results in Fig. 12 show the model defined by Owen et al. [14] falls short in capturing the experimentally observed trend of the inflection point. Specifically, the full-span and part-span experimental data both yield a high-order nonlinear trend, which is best represented by a large Γ_c value (a nearly linear model prediction). The value of $\Gamma_c = 5.2$ used in Fig. 12 represents an empirically determined fit for part-span data, as presented by Clark et al. [1], although the agreement of full-span and part-span data in Fig. 12 shows a goodness of fit with this discharge coefficient ratio, which is on par with the full-span data.

If the model selected here is to be used by engine designers to assess seal design performance, it is appropriate to evaluate its predictive capability. While the selected model overpredicts sealing capability for midrange flows, the true measured sealing effectiveness outperforms the prediction for flows, which are near the fully purged condition. Specifically, the data in Fig. 12 suggest that a reduction of nearly 30% purge flow rate from the fully purged condition may only yield a seal performance degradation of approximately 10%, versus the nearly 20% degradation predicted by the model. As engine design goals continue to seek optimized cooling schemes with decreased cooling flow requirements, this observation provides great value for hot section durability designers by showing that purge flow reductions may be acceptable with limited decrease of seal performance.

Moving inboard to the rim cavity region, the data from position B are presented in Fig. 13 using the same definitions in Eqs. (5) and (6). Using the same value of $\Gamma_c = 0.98$ identified by Clark et al. [1], both the part-span and full-span data show good qualitative agreement with each other and the predictive model. The discussion by Clark et al. suggests this agreement is a function of the geometry and the value of Γ_c near unity, which is more representative of other similar studies in the open literature. The

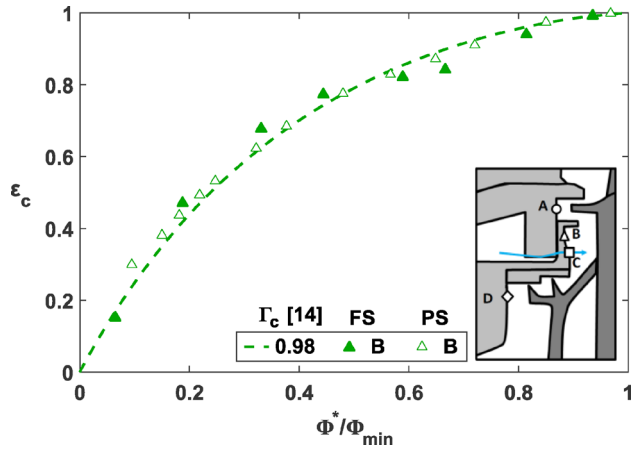

Fig. 13 Empirical model for sealing effectiveness [14] compared with experimental data for outer rim cavity (location B)

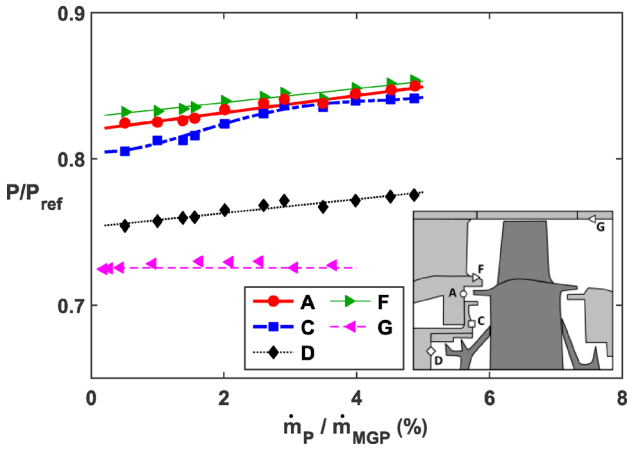

Fig. 15 Nondimensional pressures for FS configuration identifying flow-driving pressure differentials

side-by-side comparison of locations A and B with the orifice-based model [14] simultaneously highlights the value and limitations of such predictive tools.

Recalling the differences noted in Fig. 8, the inboard measurement locations (C and D) show the most significant discrepancies between the full-span and part-span sealing effectiveness data at low purge flow rates. To further address these discrepancies, those two locations are recast in Fig. 14 using the same normalized sealing flow parameter defined in Eq. (6). The correlation is not included in Fig. 14 due to the lack of model comparison shown by Clark et al. [1] at these positions.

At low flow rates, the full-span sealing effectiveness in Fig. 14 is as much as 60% lower than the part-span data, signifying the sealing capability of the purge flow is no longer effective, and high-temperature main gas path fluid is reaching far down into the rim cavity and the front wheel space.

The shift observed at low flow rates in Fig. 14 is further evaluated using pressure differentials as a driving potential for flow. Figure 15 shows the same nondimensional full-span pressure data from Fig. 9, but additional measurements in the main gas path supplement further discussion. A comparison is drawn with pressures for part-span data in Fig. 16. For the full-span configurations, Fig. 15 shows the pressure in the front wheel-space cavity (location D) is significantly lower than the rim cavity region (location C). This observation is in contrast with the part-span geometry, for which location D trends much closer to location C in Fig. 16.

As noted earlier, the change of test section configuration from part-span blades to full-scale engine blades also led to the inclusion of film cooling holes on the blades, which were not present for the simplified part-span blades. As a result, there is an available flow route (radially inward from location A toward C and D, through the cover plates, and out through the blade cooling holes), which was not present for the part-span configuration—see Fig. 17(*a*). This flow route is supported by the cavity pressures in Fig. 15, in combination with a static pressure downstream of the rotor, location G, which is consistently lower than the front wheel-space cavity, D.

The absence of this route for the part-span geometry leads to a pressurization of the front wheel space, causing the higher effectiveness measurements for the part-span geometries in Fig. 14. As the purge flow rate increases, the pressure builds at location D, and the pressure converges toward the rim seal pressure (Fig. 16). Because both the part- and full-span geometries represent engine-realistic designs with fir tree blade attachments, potential leak paths exist through these fir trees and between the blades, Figs. 17(*a*) and 17(*b*). However, these leak paths are less significant than the path through the blade cooling holes due to the fact that the aft wheel-space region is typically at a higher presser than the main gas path.

In contrast, the cooling hole leakage path identified in Fig. 17(*a*) for the full-span configuration leads to hot gas ingestion into the front wheel-space cavity, effectively decreasing the

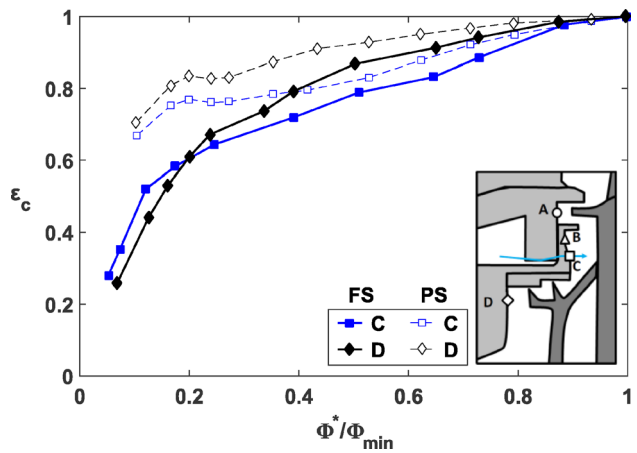

Fig. 14 Sealing effectiveness at inner radial locations as a function of net sealing flow rate

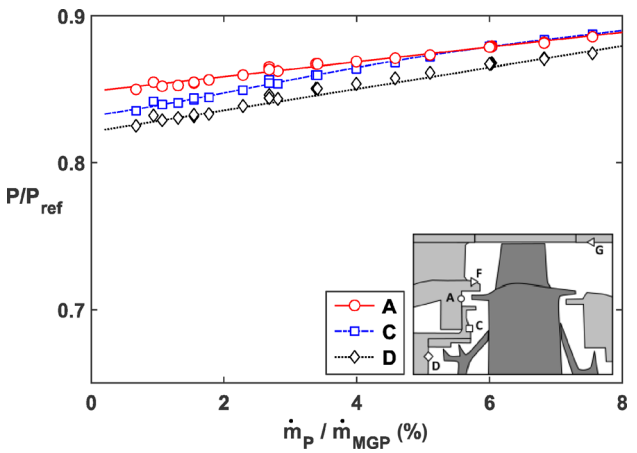

Fig. 16 Nondimensional pressures for PS configuration identifying flow-driving pressure differentials

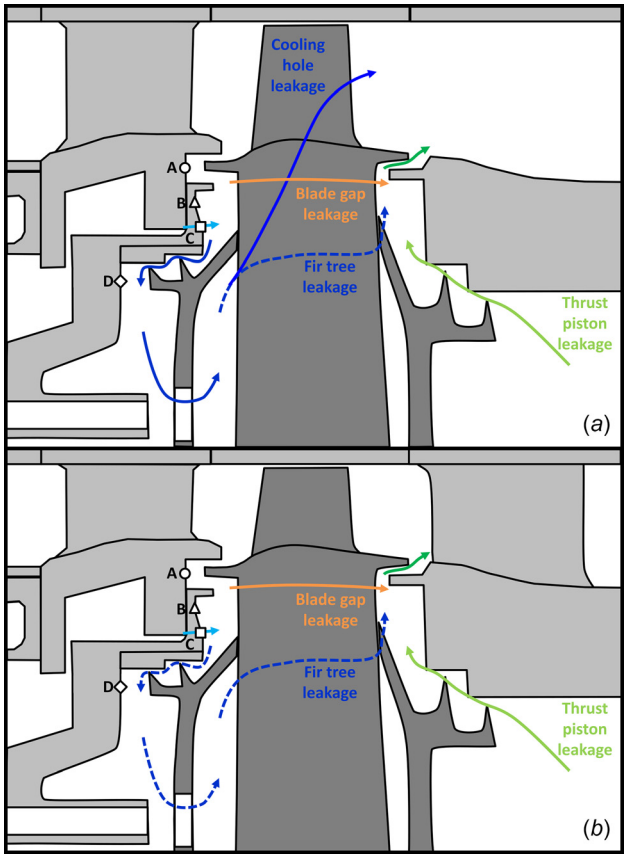

Fig. 17 Schematic of secondary flow paths without TOBI flow: (*a*) blade cooling holes present (FS) and (*b*) blade cooling holes absent (PS)

sealing performance at that location. Furthermore, the full-span configuration shows the front wheel-space cavity pressure (location D) diverges from the rim seal pressure (location A) as purge flow rate increases.

For typical gas turbine engine operation, the blade cooling holes would be fed by TOBI flow, which would negate these observed trends at locations C and D. However, in spite of these limitations, it is important to note that both of the turbine configurations compared in this study identified identical trends of sealing effectiveness in the critical rim seal zone (location A) and the outer rim cavity (location B), as shown in Figs. 12 and 13. In other words, the sealing behavior and flow patterns observed far inboard do not directly influence the behavior of the critical rim seal. As a result, the use of part-span turbine hardware [1] is validated for assessing rim seal performance.

Summary and Conclusions

In this study, data were collected from a one-stage turbine facility operating at engine-representative conditions with true-scale engine airfoils and seal geometries. Using CO_2 as a tracer gas, sealing effectiveness was quantified to assess whether differences occur as a result of the changes to blade span. Sealing effectiveness values and scaling were compared between full-span and previously reported part-span blades and vanes.

A direct comparison of full- and part-span hardware showed that the ratio of purge flow to main gas path flow does not scale sealing effectiveness levels when airfoil span changes. This result is expected considering that there is no reason to believe the amount of purge flow required for the rim seal would increase only due to an increase in the main gas path flow, which would be required for an increased airfoil span. This study also showed that the relative rotor tip clearance had no effect on the measured sealing effectiveness throughout the rim cavity zone.

Using a nondimensional flow parameter, the sealing effectiveness values for both the full-span and part-span airfoils scaled well. However, the sealing effectiveness values did not always agree with a theoretical model based on ingress and egress discharge coefficients. For both full- and part-span airfoils, measured effectiveness levels in the outer rim cavity aligned well with the theoretical model, but measurements in the rim seal region indicated an inflection point in the sealing effectiveness that is not represented in the theoretical model. This inflection point occurred as the purge flow was increased resulting in the cavity pressure approaching the rim seal pressure. Despite this inconsistency with the model, the measured gas concentrations show that if an engine design is currently operating near a fully purged rim seal configuration without TOBI flow, a relatively small reduction of purge flow may lead to less degradation of sealing effectiveness than predicted by the model.

These results showed overall that a change of airfoil span does influence the absolute amount of purge flow required to fully seal the rim cavity. However, the trends of a scaled sealing effectiveness as a function of flow rate do not change if the appropriate method is used to scale the data. Furthermore, the presence or absence of blade cooling holes in the airfoils had no effect on the measured sealing effectiveness in the rim seal and rim cavity regions. As long as the fully purged flow rate is known, differing airfoil spans and simplified cooling geometries can be used to describe the behavior of a given seal geometry.

This study has addressed several important questions related to the influence of blade span and rotor tip clearance on the sealing effectiveness of turbine rim cavity purge flow. Knowledge of the influence from these contributors both independently and together helps drive development of new theoretical ingress/egress models and advanced predictive algorithms benefitting future aggressive engine designs. The data presented in this study point toward important follow-on work assessing the influence of TOBI flow with and without purge flow when cooling holes are present in the blades.

Acknowledgment

The authors would like to recognize and thank Pratt & Whitney, the U.S. Department of Energy National Energy Technology Laboratory, and the U.S. Federal Aviation Administration for sponsoring research presented in this paper.

Funding Data

- National Energy Technology Laboratory (DE-FE0025011, Funder ID. 10.13039/100013165).

Nomenclature

b = hub radius
c = gas concentration
$C_{d,i}, C_{d,e}$ = discharge coefficient for ingress, egress
FP = flow parameter, $\dot{m}_P\sqrt{T_t}/P_tN$
$\dot{m}$ = mass flow rate
N = number of purge holes
P = pressure
PR = stage pressure ratio
Re_x = axial Reynolds number, VC_x/ν
Re_ϕ = rotational Reynolds number, $\Omega b^2/\nu$
s = wetted surface distance
S = nondimensional annulus span
T = temperature
Γ_c = ratio of discharge coefficients, $C_{d,i}/C_{d,e}$
ε_c = sealing effectiveness, $(c - c_\infty)/(c_s - c_\infty)$

ρ = density
τ = rotor tip clearance
Φ = nondimensional sealing flow parameter
Φ_0 = largest flow parameter with zero effectiveness
Φ_{min} = minimum flow parameter to seal a given location
Φ^* = net sealing flow rate, $\Phi - \Phi_0$
Ω = angular velocity

Subscripts, Accents, and Abbreviations

avg = area-weighted average
FS = full-span
max = maximum
MGP = main gas path
P = purge
PS = part-span
ref = generic reference condition
s = supply level
t = total condition
∞ = background level
$\hat{}$ = normalized value

References

[1] Clark, K., Barringer, M., Johnson, D., Thole, K., Grover, E., and Robak, C., 2018, "Effects of Purge Flow Configuration on Sealing Effectiveness in a Rotor-Stator Cavity," ASME J. Eng. Gas Turbines Power, **140**(11), p. 112502.
[2] Scobie, J. A., Sangan, C. M., Owen, J. M., and Lock, G. D., 2016, "Review of Ingress in Gas Turbines," ASME J. Eng. Gas Turbines Power, **138**(12), p. 120801.
[3] Johnson, B. V., Mack, G. J., Paolillo, R. E., and Daniels, W. A., 1994, "Turbine Rim Seal Gas Path Flow Ingestion Mechanisms," AIAA Paper No. 94-2703.
[4] Bayley, F. J., and Owen, J. M., 1970, "The Fluid Dynamics of a Shrouded Disk System With a Radial Outflow of Coolant," J. Eng. Power, **92**(3), pp. 335–341.
[5] Phadke, U. P., and Owen, J. M., 1988, "Aerodynamic Aspects of the Sealing of Gas Turbine Rotor-Stator Systems—Part 1: The Behavior of a Simple Shrouded Rotating-Disk Systems in a Quiescent Environment," Int. J. Heat Fluid Flow, **9**(2), pp. 98–105.
[6] Owen, J. M., 2011, "Prediction of Ingestion Through Turbine Rim Seals—Part I, Rotationally-Induced Ingress," ASME J. Turbomach., **133**(3), p. 031005.
[7] Owen, J. M., 2011, "Prediction of Ingestion Through Turbine Rim Seals—Part II: Externally-Induced and Combined Ingress," ASME J. Turbomach., **133**(3), p. 031006.
[8] Sangan, C. M., Pountney, O. J., Zhou, K., Wilson, M., Owen, J. M., and Lock, G. D., 2013, "Experimental Measurements of Ingestion Through Turbine Rim Seals—Part I: Externally-Induced Ingress," ASME J. Turbomach., **135**(2), p. 021012.
[9] Sangan, C. M., Pountney, O. J., Zhou, K., Wilson, M., Owen, J. M., and Lock, G. D., 2013, "Experimental Measurements of Ingestion Through Turbine Rim Seals—Part II: Rotationally-Induced Ingress," ASME J. Turbomach., **135**(2), p. 021013.
[10] Scobie, J. A., Hualca, F. P., Patinios, M., Sangan, C. M., Owen, J. M., and Lock, G. D., 2018, "Re-Ingestion of Upstream Egress in a 1.5-Stage Gas Turbine Rig," ASME J. Eng. Gas Turbines Power, **140**(7), p. 072507.
[11] Barringer, M., Coward, A., Clark, K., Thole, K., Schmitz, J., Wagner, J., Alvin, M. A., Burke, P., and Dennis, R., 2014, "Development of a Steady Thermal Aero Research Turbine (START) for Studying Secondary Flow Leakages and Airfoil Heat Transfer," ASME Paper No. GT2014-25570.
[12] Clark, K., Barringer, M., Thole, K., Clum, C., Hiester, P., Memory, C., and Robak, C., 2017, "Effects of Purge Jet Momentum on Sealing Effectiveness," ASME J. Eng. Gas Turbines Power, **139**(3), p. 031904.
[13] Clark, K., Barringer, M., Thole, K., Clum, C., Hiester, P., Memory, C., and Robak, C., 2016, "Using a Tracer Gas to Quantify Sealing Effectiveness for Engine Realistic Rim Seals," ASME Paper No. GT2016-58095.
[14] Owen, J. M., Zhou, K., Pountney, O. J., Wilson, M., and Lock, G., 2012, "Prediction of Ingress Through Turbine Rim Seals—Part I: Externally Induced Ingress," ASME J. Turbomach., **134**(3), p. 031012.